UC San Diego

UC San Diego Previously Published Works

Title

Seasonal Shift in the Dominant Pathway Energizing Mesoscale Eddies in the California Current

Permalink

https://escholarship.org/uc/item/89j3r2gz

Journal

Journal of Physical Oceanography

ISSN

0022-3670

Authors

Gazeley, Jack F

Gille, Sarah T

Siegelman, Lia

et al.

Publication Date

2026-09-22

DOI

10.1175/jpo-d-26-0092.1

Copyright Information

This work is made available under the terms of a Creative Commons Attribution License, available at https://creativecommons.org/licenses/by/4.0/

Peer reviewed

eScholarship.org Powered by the California Digital Library
University of California

Generated using the official AMS LaTeX template v6.1

Seasonal Shift in the Dominant Pathway Energizing Mesoscale Eddies in the California Current

Jack F. Gazeley[a] , Sarah T. Gille[a] , Lia Siegelman[a] , Alberto C. Naveira Garabato[b] , Jackie May[c] , Joseph D'Addezio[c] , Shang-Ping Xie[a]

[a] *Scripps Institution of Oceanography, University of California, San Diego, California, US*

[b] *Ocean and Earth Science, National Oceanography Centre, University of Southampton, Southampton, UK*

[c] *U.S Naval Research Laboratory, Ocean Sciences Division, Stennis Space Center, Mississippi, US*

Corresponding author: Jack F. Gazeley, jgazeley@ucsd.edu

ABSTRACT: Mesoscale eddies are the dominant reservoir of kinetic energy in the ocean, yet the mechanisms that generate and maintain them in eastern boundary current systems remain incompletely assessed. Here we use a 1-km resolution simulation of the California Current System (CCS) to diagnose and quantify the processes that supply kinetic energy to the mesoscale band. A pronounced seasonal transition is evident in surface vorticity, kinetic energy spectra, and mixed-layer depth. In winter and spring, the mixed layer deepens during periods of strong wind work. Once the forcing relaxes, the mixed layer restratifies, generating submesoscale eddies and filaments. These features merge and transfer energy upscale, supplying the mesoscale through an inverse cascade. These mixed-layer restratification events occur most frequently when the mixed layer is deep (~50 m) and highly variable. In contrast, during summer when the mixed layer is shallow, a mixed-layer-averaged geostrophic kinetic energy budget indicates that wind work accelerates the surface layer of the ocean more efficiently. This is associated with enhanced kinetic energy transfer from scales larger than 100 km into the mesoscale. Together, these results indicate a seasonally varying balance between inverse and direct kinetic energy transfers in the CCS, implying that the annual cycle of upper-ocean stratification leads to a seasonal shift in the dominant pathway of mesoscale eddy generation.

SIGNIFICANCE STATEMENT: Upper-ocean stratification influences ocean surface currents through multiple mechanisms, but the relative importance of these mechanisms has not been quantified. Stronger stratification can trap wind forcing in a shallow layer and accelerate surface currents, while weaker stratification increases available potential energy variance and promotes submesoscale instabilities. In this study, we show that both mechanisms are important in the dynamics of the California Current System but dominate at different times of year and at different scales. In summer, shallow mixed layers favor accelerated surface currents and a forward cascade from larger scales. In winter and spring, mixed-layer instabilities energize the mesoscale through an inverse cascade. Additionally, the importance of the inverse cascade implies that unresolved submesoscale motions can influence mesoscale variability and therefore have consequences for ocean predictability.

1. Introduction

The mesoscale eddy field, with horizontal scales of $O(100)$ km, accounts for up to 80% of the kinetic energy in the global ocean (Ferrari and Wunsch 2009). Mesoscale eddies play a central role in transporting tracers and regulating marine ecosystems by modulating nutrient supply and biological productivity (McGillicuddy et al. 2007). They dominate lateral stirring and set the effective diffusivity of tracers in the ocean (Ferrari and Nikurashin 2010). The mesoscale circulation also governs the structure of wave–eddy interactions, controlling the transmission of internal wave energy into the ocean interior and its subsequent contribution to diapycnal mixing (Asselin and Young 2020). The oceanic mesoscale is an essential component of air–sea interactions, biophysical coupling, and the global kinetic energy budget. Yet, despite the oceanic mesoscale's importance, the relative contributions of the processes that generate and maintain mesoscale energy have not been fully reconciled across different circulation regimes, particularly on seasonal-to-interannual timescales.

The prevailing paradigm is that oceanic mesoscale kinetic energy is generated and maintained through a combination of large-scale forcing and cross-scale kinetic energy cascades, rather than by direct forcing at mesoscale wavelengths alone. At leading order, mesoscale eddies are traditionally understood to draw energy from the large-scale circulation through baroclinic instability, converting available potential energy associated with mean buoyancy gradients into eddy kinetic energy at

scales of order of the first baroclinic Rossby radius (Vallis 2017; Ferrari and Wunsch 2009). This injection feeds a predominantly downscale direct cascade of kinetic energy toward smaller scales and ultimately dissipation, consistent with classical views of geostrophic turbulence (Charney 1971; Vallis 2017). In this framework, energy is input into the ocean primarily by wind forcing at large spatial scales, typically exceeding 250 km (Rai et al. 2021). Recent work further suggests that the efficiency of this large-scale wind-driven momentum input may depend on upper-ocean stratification, with surface currents more readily accelerating when mixed layers are shallow, since the same wind stress can be more efficiently transferred into a layer with less inertia (Peng et al. 2022). Such modulation of the large-scale flow has the potential to influence the amount of kinetic energy available for mesoscale baroclinic instability and the direct cascade, thereby affecting the energization of the mesoscale. However, a quantitative assessment of the relative importance of this pathway in setting mesoscale energetics has yet to be established.

In contrast, high-resolution numerical simulations and observations have demonstrated that significant energy can also be injected at submesoscales through mixed-layer instabilities (MLIs). Episodes of rapid mixed-layer deepening followed by restratification are frequently accompanied by an injection of submesoscale kinetic energy (Boccaletti et al. 2007; Sasaki et al. 2014; Fox-Kemper et al. 2008) that can transfer upscale through an inverse cascade and merge into the mesoscale band (Schubert et al. 2020; Sasaki et al. 2014). The seasonality of the submesoscale structures is strongly modulated by the seasonal cycle in mixed-layer depth (MLD) via MLIs (Brannigan et al. 2015; Callies et al. 2015; Rocha et al. 2016; Sasaki et al. 2014; Qiu et al. 2014). During winter and early spring, surface cooling and enhanced wind forcing deepen the mixed layer and weaken stratification, allowing strong lateral buoyancy gradients to persist within the mixed layer (Holte et al. 2017; Zhang et al. 2018). These conditions are conducive to the growth of MLIs, which act to restratify the mixed layer and smooth horizontal buoyancy gradients through ageostrophic motions (Boccaletti et al. 2007; Fox-Kemper et al. 2008). Some studies have hypothesized that the pronounced seasonal variability of submesoscale activity may also contribute to the seasonal cycle of mesoscale kinetic energy through an inverse kinetic energy cascade (Sasaki et al. 2014; Qiu et al. 2014; Naveira-Garabato et al. 2022; Khatri et al. 2021). In contrast, other work has emphasized that submesoscale variability exhibits a strong seasonal cycle even in regions where mesoscale energy shows comparatively weak seasonality (Callies et al. 2015; Buckingham et al.

2016). However, a systematic quantification of the cumulative contribution of MLI-driven inverse transfers to the mesoscale energy budget, and a direct comparison of this pathway with the classical mesoscale baroclinic instability of the large-scale flow, has not yet been established. In particular, the relative importance of these two pathways under different stratification and forcing regimes remains an open area of research.

The California Current System (CCS) is an eastern boundary current characterized by strong seasonal variability in surface forcing and stratification. The CCS undergoes a pronounced seasonal cycle associated with storm activity and upwelling, which drives large variations in mixed-layer depth, surface buoyancy fluxes, and alongshore wind stress (Di Lorenzo 2003). These seasonal changes are accompanied by substantial reorganization of the surface circulation. In winter and early spring, persistent upwelling-favorable winds maintain sloped coastal isopycnals that support a strong equatorward jet, while the coastal poleward return flow is absent. As upwelling relaxes in summer, positive wind-stress curl over the continental slope drives the development of a pronounced poleward return flow, a transition well documented in climatological observations (Di Lorenzo 2003). This adjustment is associated with a flattening of coastal isopycnals and the offshore propagation of mesoscale features in the form of westward-propagating Rossby waves generated by baroclinic instability of the mean flow. High-resolution observations have demonstrated that the CCS supports energetic variability across a wide range of scales, including both mesoscale eddies and vigorous submesoscale motions (Torres et al. 2024; Farrar et al. 2025). Capet et al. (2008c) analyzed a hierarchy of primitive-equation simulations of an idealized, subtropical eastern-boundary upwelling system resembling the CCS, run at successively finer resolution from 12 to 0.75 km under steady, idealized upwelling-favorable forcing. Across the resolved submesoscale they found a robust forward KE cascade, in which mesoscale straining drives surface frontogenesis and ageostrophic secondary circulation that fluxes energy downscale to dissipation. In these models, the submesoscale therefore acts predominantly as a sink of mesoscale energy rather than as a source. This stands in apparent contrast to the MLI pathway invoked in other regions (e.g., Sasaki et al. 2014; Qiu et al. 2014; Naveira-Garabato et al. 2022), in which MLIs generate submesoscale eddies whose energy is transferred upscale into the mesoscale through an inverse cascade. The contrast between these two pictures highlights a gap in our understanding of how the

mesoscale is energized in the CCS. Here we address this gap with a complex, data-assimilating simulation of the CCS at 1 km resolution and realistic atmospheric forcing.

Despite substantial progress on both mixed-layer instability dynamics and mean-flow baroclinic instability in boundary current systems, a clear gap remains in quantifying how these pathways jointly contribute to the mesoscale kinetic energy in the CCS, and how their relative importance varies seasonally. In this study, we address this problem using a 1-km resolution simulation of the CCS from March–October 2023. We first characterize the seasonal evolution of the ocean dynamics and their energetics in the CCS in Section 3a. We then examine the mechanisms driving MLIs and their associated submesoscale energy injection using a composite of more than 300 events in Section 3b. In Section 3c, we demonstrate that large-scale forcing of the circulation is dominated by wind-driven momentum trapping during the shallow mixed layer season, by considering a geostrophic mixed-layer averaged budget. Finally, in Section 3d, we compare and quantify the relative importance of these two mechanistic pathways in supplying kinetic energy via inverse and direct kinetic energy cascades to the mesoscale band over the annual cycle, using a coarse-grained cross-scale kinetic energy transfer diagnostic framework. Section 4 discusses the implications of the work after summarizing and contextualizing within the existing literature.

2. Data and Methods

a. Data

The Coupled Ocean Atmosphere Modelling Prediction System (COAMPS, Allard et al. 2015) version 2021.1 is used in this study. COAMPS includes modelling components representing the ocean, atmosphere, waves, and ice and has the ability to run these components in a stand-alone or coupled configuration. For this study, only the ocean component, the Navy Coastal Ocean Model (NCOM, Barron et al. 2006), is run as a stand-alone system over the CCS region. The modelled domain extends from 230° –244.5° W and 30°–42°N with a 1-km horizontal resolution. There are 100 vertical levels with 36 terrain following sigma layers on top of 64 constant depth levels (z-levels), with the transition between the sigma and z-levels occurring at 150 m. The surface sigma layer is 1.5 m thick with continuous stretching applied to subsequent layers, extending to a maximum ocean bottom depth of 5500 m.

NCOM is a primitive equation model that uses the hydrostatic and Boussinesq approximations. In this study, NCOM utilizes the Mellor and Yamada (1982) level-2 vertical mixing scheme and the Smagorinsky (1963) horizontal diffusion scheme. Horizontal boundary conditions were obtained from 3 h output from the 1/12° horizontal resolution Global Ocean Forecasting System (GOFS, Metzger et al. 2015) version 3.5. Atmospheric forcing fields were provided with a frequency of 3 h by the 0.5° horizontal resolution global atmospheric model, NAVy Global Environmental Model (NAVGEM, Hogan et al. 2015). Fresh water river in flow fluxes were estimated from the NCOM monthly climatology river data base (Barron and Smedstad 2002). NCOM barotropic tidal forcing was applied using the global Oregon Tidal Inverse Solution (OTIS, Egbert and Erofeeva 2002). Barotropic tidal interactions with bathymetry introduce baroclinic tides into the simulation.

Ocean data assimilation is performed daily at 00z with the Navy Coupled Ocean Data Assimilation (NCODA) three-dimensional variational (3DVAR) analysis system (Daley and Barker 2001; Cummings et al. 2010; Cummings 2005). Observations that are assimilated include temperature, salinity, and sea surface height anomalies (SSHA). Temperature and salinity profiles are obtained from in situ platforms; SSHA observations are obtained from the nadir altimeters onboard the Joint Altimetry Satellite Oceanography Network (JASON)-3, Sentinel-3A, Sentinel-3B, and Satellite with ARgos and ALtika (SARAL) platforms; and sea surface temperature (SST) observations are obtained from ships, buoys, floats and satellite sensors onboard the Meteorological operational satellite (Metop)-C, National Oceanic and Atmospheric Administration (NOAA)-20, and Suomi National Polar-orbiting Partnership (S-NPP) platforms. The data assimilation window is set to 48 h for in situ profiles, 120 h for nadir altimeters, and 24 h for SST. This single-scale configuration of NCODA-3DVAR is expected to only correct for large, mesoscale ocean features, leaving smaller submesoscales mostly unaltered during the update cycle (D'Addezio et al. 2019).

b. Mixed-Layer Depth

The mixed-layer depth (MLD) is used in this study to characterize the seasonal cycle in stratification and forcing, define and detect deepening–restratification events that energize submesoscale motions (Section 3b), and interpret the seasonal transition in mesoscale forcing and eddy scale (Section 3d). Here we define the MLD following Reichl et al. (2022), as the depth of uppermost layer that reaches a pre-defined potential energy (PE) anomaly. The PE anomaly of a seawater layer

quantifies the wind work required to homogenize its density. The MLD is defined as the depth at which the simplified PE anomaly of the layer equals a prescribed value, ϕ:

$$\phi = \int_{-h}^{\eta} (\rho_m - \rho_i) g z \, dz, \tag{1}$$

where

$$\rho_m = \frac{1}{\eta + h} \int_{-h}^{\eta} \rho_i \, dz, \tag{2}$$

is the density the layer would have if fully mixed, i.e., the mean density within the layer. Equation 1 can be inverted for h for a given ϕ using a Newton–Raphson algorithm (Reichl et al. 2022). However, it is often computationally cheaper to compute the simplified PE anomaly for all possible values of h and interpolate to the target value of ϕ. The PE anomaly method requires specifying a value of ϕ, which was empirically tuned using wind-work diagnostics following Reichl et al. (2022).

c. Wavenumber–Frequency Spectrum

Wavenumber and wavenumber–frequency spectra are used in Section 3a to quantify how the energetic distribution across scales and frequencies changes between winter/spring and summer. The isotropic wavenumber–frequency ($\omega - k$) spectrum is calculated in a ~860 km × 1300 km box that does not include the coast. The data are segmented into 430 km × 430 km × 360 hour bins, with 50% overlap in both time and space, resulting in a total of 77 segments for each of the two month periods March–April and August–September. The mean and linear trend in each dimension of each segment are then removed, and a 3-D Hanning window is applied before taking the 3-D Fast Fourier Transform (FFT). The Fourier transformed segments are averaged, and the squared amplitude of the average is normalized in order to satisfy Parseval's Theorem. This results in a 3-D spectrum in k_x, k_y and ω. However, to reduce to a 2-D isotropic $\omega - k$ spectrum, the spectral energy corresponding to each $k = \sqrt{k_x^2 + k_y^2}$ is summed. The full details of this method are described by Torres et al. (2018).

d. Coarse-Graining

The coarse-graining method (Aluie et al. 2018) provides a framework for deriving a scale-dependent kinetic energy budget in fluid flows. The coarse-grained kinetic energy flux Π is used in this study to diagnose cross-scale kinetic energy transfer. This will provide evidence for inverse transfers following MLIs, and for a seasonally varying partition of the mesoscale energy supply from submesoscales and large scales. The cross-scale kinetic energy transfer function Π_ℓ at a scale ℓ represents the flux of kinetic energy from scales larger than ℓ to scales smaller than ℓ:

$$\Pi_\ell = -\rho_0 \overline{\mathbf{S}} : \tau_\ell, \tag{3}$$

where the colon represents the tensor double contraction operation, $\overline{\mathbf{S}} = (\nabla\overline{\mathbf{u}} + \nabla\overline{\mathbf{u}}^T)/2$ is the filtered strain tensor, and $\tau_\ell = \overline{\mathbf{u}\mathbf{u}} - \overline{\mathbf{u}}\,\overline{\mathbf{u}}$ is defined as the sub-filter stress tensor. More details about the filtering and this derivation can be found in Aluie et al. (2018).

The total amount of kinetic energy transferred across a given scale ℓ can be calculated by integrating Π_ℓ over the whole spatial domain D and time:

$$\Delta E_{\text{cascade}}(t) = -\int_{t_0}^{t}\int_D \Pi_\ell(x, y, z, t)\; dx\; dy\; dz\; dt, \tag{4}$$

where $\Delta E_{\text{cascade}}(t)$ represents the total amount of energy gained by scales larger than ℓ from scales smaller than ℓ over the time period from t_0 to t.

e. Dynamical Filtering

The dynamical filter is used in Section 3b to define submesoscale kinetic energy as a balanced component separated from internal gravity waves (IGWs) and then split by a low-pass spatial filter. A Butterworth filter at the boundary of the IGW spectrum and the balanced motions can be derived from the IGW dispersion relation. For a more detailed discussion of this method, see Torres et al. (2022). In this study, the dynamical filter is applied on a box of size ~500 km × 1300 km in the offshore region, and the balanced motions are further separated into submesoscale and mesoscale components using a 25-km low-pass filter. This scale is chosen to be of the same order as the first baroclinic Rossby radius of deformation in the region (Chelton et al. 1998).

f. Geostrophic Mixed-Layer-Averaged Kinetic Energy Budget

The geostrophic mixed-layer-averaged kinetic energy budget is used in Section 3c to quantify the seasonal balance between wind work per unit mixed-layer depth and ageostrophic–geostrophic energy transfer, and to relate this to the seasonal supply of energy into the mesoscale band. The budget is calculated by taking the mixed-layer average of the incompressible, rotating Boussinesq equations to generate a momentum budget, separating the velocity into geostrophic and ageostrophic components, and then taking the dot product with the geostrophic mixed-layer-averaged velocity to generate the kinetic energy budget. The 25-km filter scale used to separate the mesoscale and submesoscale matches the first baroclinic Rossby radius (Section 2e), the larger-scale flow it isolates is low-Rossby-number (Fig. 1) and predominantly geostrophic, justifying our use of $\mathbf{U}_g$ as a proxy for the mesoscale and larger-scale flow. Starting from the incompressible rotating Boussinesq equations

$$\partial_t \mathbf{u} + \mathbf{u}\cdot\nabla\mathbf{u} = -\frac{\nabla P}{\rho_0} - f\hat{\mathbf{z}}\times\mathbf{u} + \frac{1}{\rho_0}\partial_z\tau, \tag{5}$$

we can average over the depth of the mixed layer, i.e, apply the operation $h^{-1}\int_{-h}^{0}[\cdot]dz$ to each term in the momentum equations, resulting in

$$\frac{D\mathbf{U}}{Dt} + f\hat{\mathbf{z}}\times\mathbf{U} = -\nabla\phi + \frac{\tau_\mathbf{s}}{\rho_0 h} + \frac{\nabla h\cdot p(-h)}{h\cdot\rho_0}. \tag{6}$$

Additional terms appear from the Leibniz integral rule when mixed-layer averaging. However, here we have assumed that $\partial_t h = w_b$, where w_b is defined as the vertical velocity at the base of the mixed layer, and $\vec{u}(z=-h)\approx\vec{U}$, i.e. there is no significant jump in velocity at the base of the mixed layer. Here, $\phi = \rho_0^{-1}h^{-1}\int_{-h}^{0}P(x,y,z,t)dz$ as defined by Boccaletti et al. (2007).

Equation 6 can be split into geostrophic and ageostrophic components such that $\mathbf{U} = \mathbf{U_g} + \mathbf{U_a}$.

$$\frac{D}{Dt}(\mathbf{U_g}+\mathbf{U_a}) = -\nabla\phi - f\hat{\mathbf{z}}\times\mathbf{U_g} - f\hat{\mathbf{z}}\times\mathbf{U_a} + \frac{\tau_\mathbf{s}}{\rho_0 h} + \frac{\nabla h\cdot p(-h)}{h\cdot\rho_0}, \tag{7}$$

but, from geostrophic balance $f\hat{\mathbf{z}}\times\mathbf{U_g} = -\nabla\phi$ and so

$$\frac{D}{Dt}(\underbrace{\mathbf{U_g}}_{(a)} + \underbrace{\mathbf{U_a}}_{(b)}) = \underbrace{-f\hat{\mathbf{z}}\times\mathbf{U_a}}_{(c)} + \underbrace{\frac{\tau_\mathbf{s}}{\rho_0 h}}_{(d)} + \underbrace{\frac{\nabla h\cdot p(-h)}{h\cdot\rho_0}}_{(e)}. \tag{8}$$

To generate a geostrophic kinetic energy budget, this equation is dotted with $\mathbf{U_g}$. Applying this to term (a) gives:

$$\mathbf{U_g} \cdot \frac{D\mathbf{U_g}}{Dt} = \frac{DK_g}{Dt}, \tag{9a}$$

where $K_g = \frac{1}{2}|\mathbf{U}_g|^2$ is the geostrophic kinetic energy. Term (b) results in

$$\mathbf{U_g} \cdot \frac{D\mathbf{U_a}}{Dt} = \mathbf{U_g} \cdot [\partial_t \mathbf{U_a} + \mathbf{U} \cdot \nabla U_a] := -\Lambda_g, \tag{9b}$$

where Λ_g can be interpreted as the work done by the ageostrophic acceleration to energize the geostrophic flow, or the ageostrophic-geostrophic kinetic energy transfer. For this to be consistent, $\Lambda_g = -\mathbf{U_g} \cdot D\mathbf{U_a}/Dt = \mathbf{U_a} \cdot D\mathbf{U_g}/Dt$, which can be shown to be true. For term (c)

$$-\mathbf{U_g} \cdot f\hat{\mathbf{z}} \times \mathbf{U_a} := \Gamma_g, \tag{9c}$$

where Γ_g is the work done by the ageostrophic vorticity on the geostrophic flow. Next, for term (d)

$$\mathbf{U_g} \cdot \frac{\tau_\mathbf{s}}{\rho_0 h} = W_g, \tag{9d}$$

where W_g is the wind work into the *geostrophic* flow per unit depth. Finally, applying the dot product with $\mathbf{U_g}$ to term (e) gives

$$\mathbf{U_g} \cdot \frac{\nabla h \cdot p(-h)}{h \cdot \rho_0} = \frac{p(-h)}{\rho_0 h} \mathbf{U_g} \cdot \nabla h. \tag{9e}$$

This term represents the work done by the geostrophic flow on fronts at the base of the ML.

So, the total budget is

$$\underbrace{\frac{DK_g}{Dt}}_{(a)} = \underbrace{\Pi_g}_{(b)+(c)} + \underbrace{W_g}_{(d)} + \underbrace{\frac{p(-h)}{\rho_0 h} \mathbf{U_g} \cdot \nabla h}_{(e)}. \tag{10}$$

where $\Pi_g = \Lambda_g + \Gamma_g$ represents total work done by the ageostrophic flow on the geostrophic flow, or the total ageostrophic-geostrophic kinetic energy transfer. In this study we hypothesize the dominant balance

$$\frac{DK_g}{Dt} = \Pi_g + W_g. \tag{11}$$

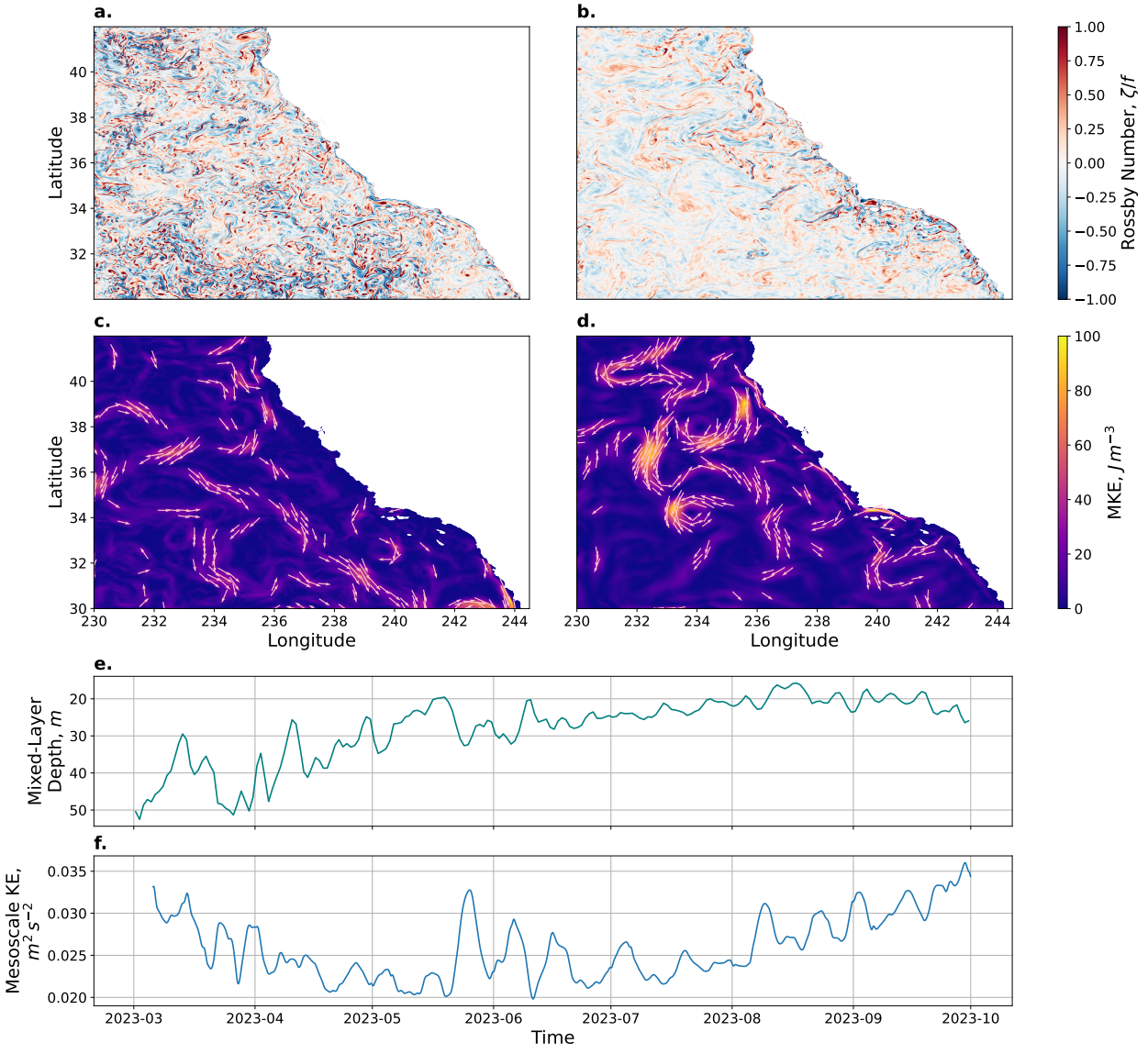
These two terms are good proxies for the two mechanisms outlined in this research.

3. Results

a. Seasonal Cycle

The surface flow of the CCS exhibits a pronounced shift in dynamical regime between late winter and late summer. Figure 1a–b compares snapshots of normalized relative vorticity ζ/f at 6-m depth in March and September. In early March (Fig. 1a), small, intense vortices and filaments, many with $|\zeta/f| \approx O(1)$ are ubiquitous throughout the domain, indicating strong submesoscale activity, particularly in the southern open-ocean region from 32–34°N. By contrast, the September field (Fig. 1b) is considerably smoother; submesoscale eddies are suppressed, and the flow is dominated by larger, more coherent mesoscale eddies with substantially lower $|\zeta/f|$. Seasonally averaged wavenumber kinetic energy spectra also reveal strong variations in eddy scale. From winter to summer, the spectral slope transitions from k^{-3} to k^{-4}, where k is the wavenumber corresponding to the scale of the features, indicating a stronger submesoscale field in winter (Fig. 2a). Additionally, more energy is present in the winter wavenumber spectrum at scales smaller than 25 km.

The monthly mean kinetic energy (MKE) of the large-scale California Current undergoes a strong seasonal cycle (Fig. 1c–d). In winter, the current is weaker and less coherent, coinciding with deeper mixed layers (Fig. 1e). By contrast, in summer the current is stronger and more coherent, flowing north–south as part of the North Pacific subtropical gyre. A coastal poleward return flow emerges in summer that is absent in winter (Fig. 1c–d). This change is consistent with climatological observations and is attributed to the seasonal upwelling cycle (Di Lorenzo 2003). These results suggest a pronounced regime shift between winter and summer. Fig. 2b shows that both the largest spatiotemporal scales and the internal gravity waves (IGWs) are more energetic during the summer months (red), whereas the submesoscale balanced motions are more intense in winter (blue). In winter, intense high-Rossby number submesoscale eddies dominate the domain (Fig. 1a), the large-scale current is weak (Fig. 1b), and the mixed layer is deep and highly variable (Fig. 1e). In summer, the flow is instead characterized by smooth, large-scale, low–Rossby number eddies (Fig. 1b), an intensified boundary current (Fig. 1d), and a shallow mixed layer (Fig. 1e). Thus, eddies in the CCS are generally small in winter and large in summer, a result of the opposing seasonal cycles of submesoscale and mesoscale kinetic energies. The existence of these two



253 FIG. 1. Instantaneous Rossby number at 6-m depth on 1 March 2023, 16:00 (a) and 30 September 2023, 16:00
254 (b). Monthly mean surface kinetic energy for March (c) and September (d), with velocity vectors plotted where
255 mean kinetic energy exceeds 75 J to illustrate the California Current System. (e) Daily domain-mean mixed-layer
256 depth. (f) Daily domain-mean kinetic energy calculated using the low-pass filtered velocity at 25 km according
257 to Section 2e.

288 contrasting states suggests that the upper ocean is not governed by a single forcing process year-
289 round, but is instead forced by multiple mechanisms, which each vary seasonally. Furthermore, the
290 domain-mean kinetic energy shows a steady decrease in mesoscale KE throughout spring, followed
291 by an increase in summer (Fig. 1f). In particular, the marked differences in eddy scale, Rossby

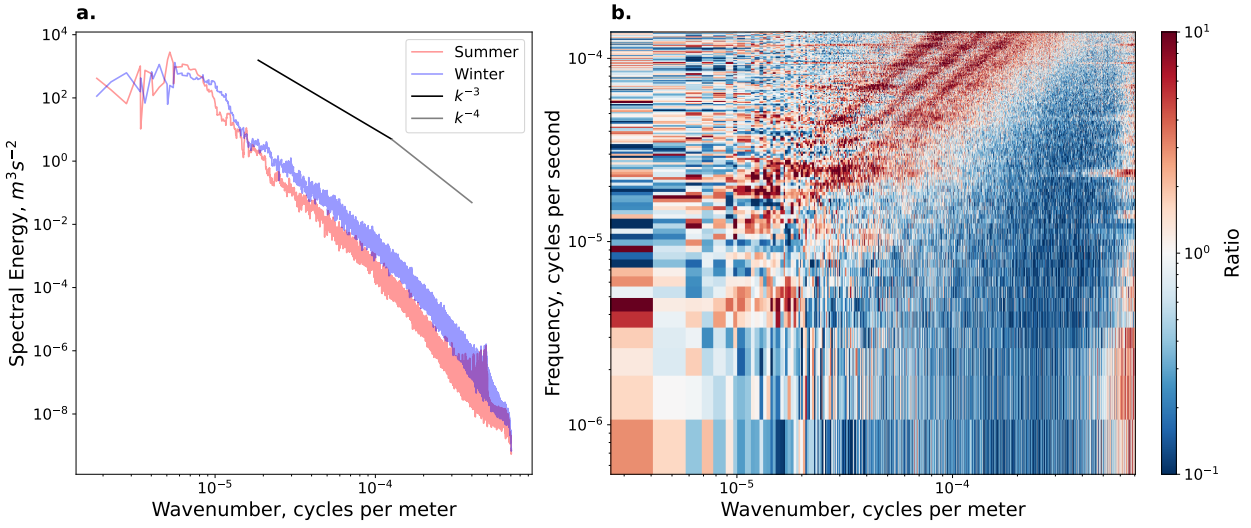


FIG. 2. a. Wavenumber KE spectra calculated in the region 230–235°E and 30–42°N for the time periods March–April (blue) and August–September (red), and spectral slopes of k^{-3} (black) and k^{-4} (gray). b. The ratio of August–September to March–April wavenumber–frequency KE spectra, where red represents enhanced energy in summer and blue represents enhanced energy in winter.

number, and mixed-layer depth imply that the mesoscale circulation is maintained by distinct forcing pathways at different points in the seasonal cycle.

b. Mixed-Layer Instabilities in the CCS

Mixed-layer instabilities are a mechanism that transfers buoyancy vertically for restratification (Boccaletti et al. 2007). In this study, we hypothesize that the seasonal cycle in CCS submesoscale kinetic energy is strongly modulated by mixed-layer instabilities that generate submesoscale eddies.

1) MLI Case Study

To illustrate the full spatio-temporal development of a single mixed-layer instability event, Figures 3–5 focus on a region of exceptionally strong storm forcing during 19–27 May 2023. Prior to the storm, the flow is dominated by moderate mesoscale variability with relatively weak submesoscale vorticity (Fig. 3a, 4a). This is followed by the passage of a strong storm (Fig. 3b, 4b), which induces intense small-scale lateral buoyancy gradients and deepens the mixed layer by 20–25m (Fig. 3c, 4c). This, in turn, results in a burst of submesoscale activity four days later, driven by frontal mixed-layer instabilities (Fig. 3d, 4d).

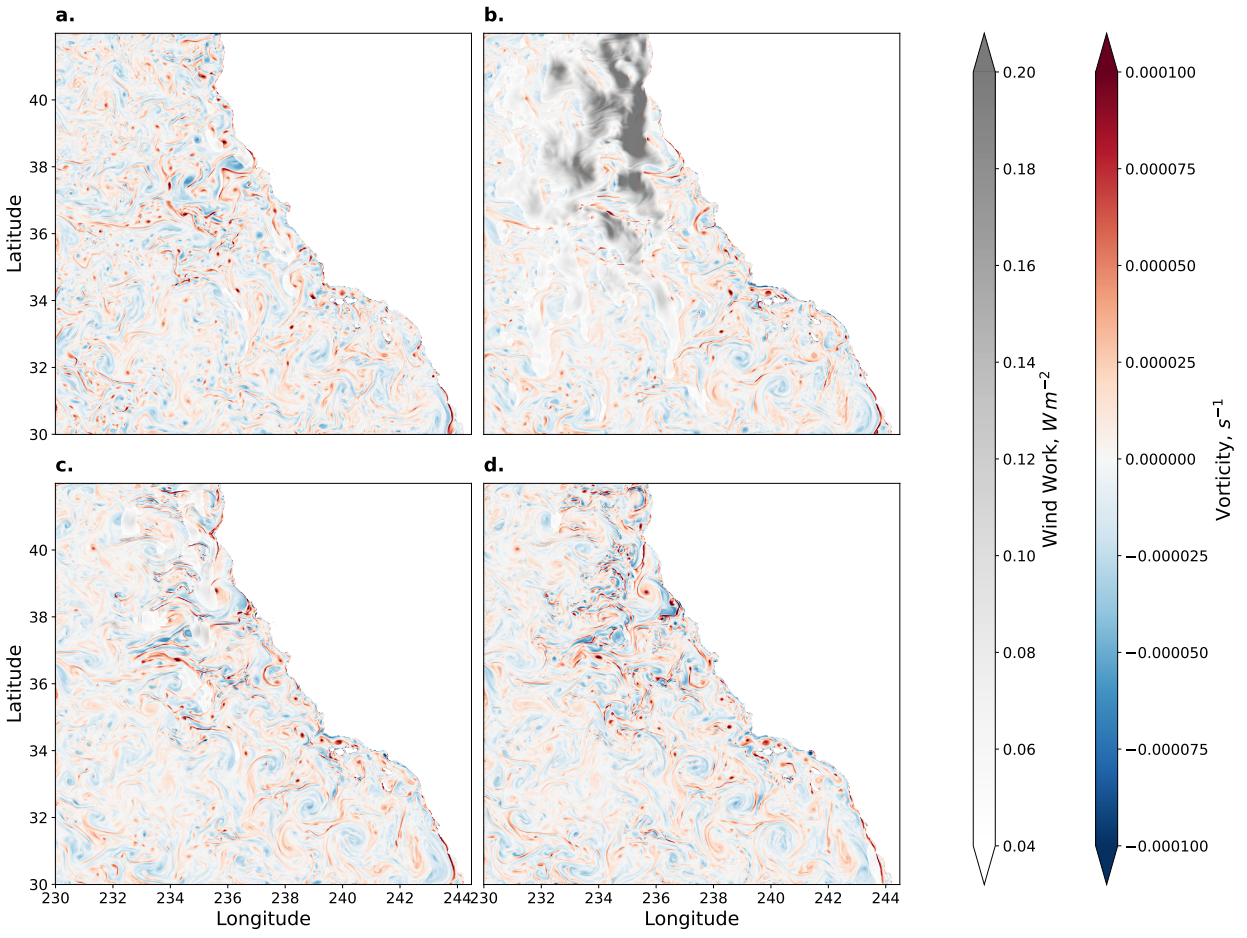


FIG. 3. Daily mean vorticity at 6 m, with wind work greater than 0.05 W m^{-2} overlaid in gray on a. 19 May 2023 b. 23 May 2023 c. 25 May 2023 d. 27 May 2023

Averaging over the full domain can obscure the signal of mixed-layer instabilities, as these processes represent localized responses to mixed-layer deepening and subsequent restratification. Focusing on the subregion where nearly all grid points experience storm-level wind forcing (Fig. 4b) allows for the construction of a more representative time series based on spatial means over this smaller domain. Figure 5 presents spatially averaged diagnostics for this subregion as a function of time. Wind work (Fig. 5a) is followed by a deepening of the mixed-layer (Fig. 5b) with a lag of approximately one day. Strong wind work is hypothesized to deepen the mixed layer by providing the mechanical energy necessary for mixing, and via buoyancy loss to the atmosphere. Subsequently, the mixed layer restratifies (Fig. 5b, after May 28). This restratification is associated with the generation of submesoscale currents, represented here as submesoscale kinetic energy,

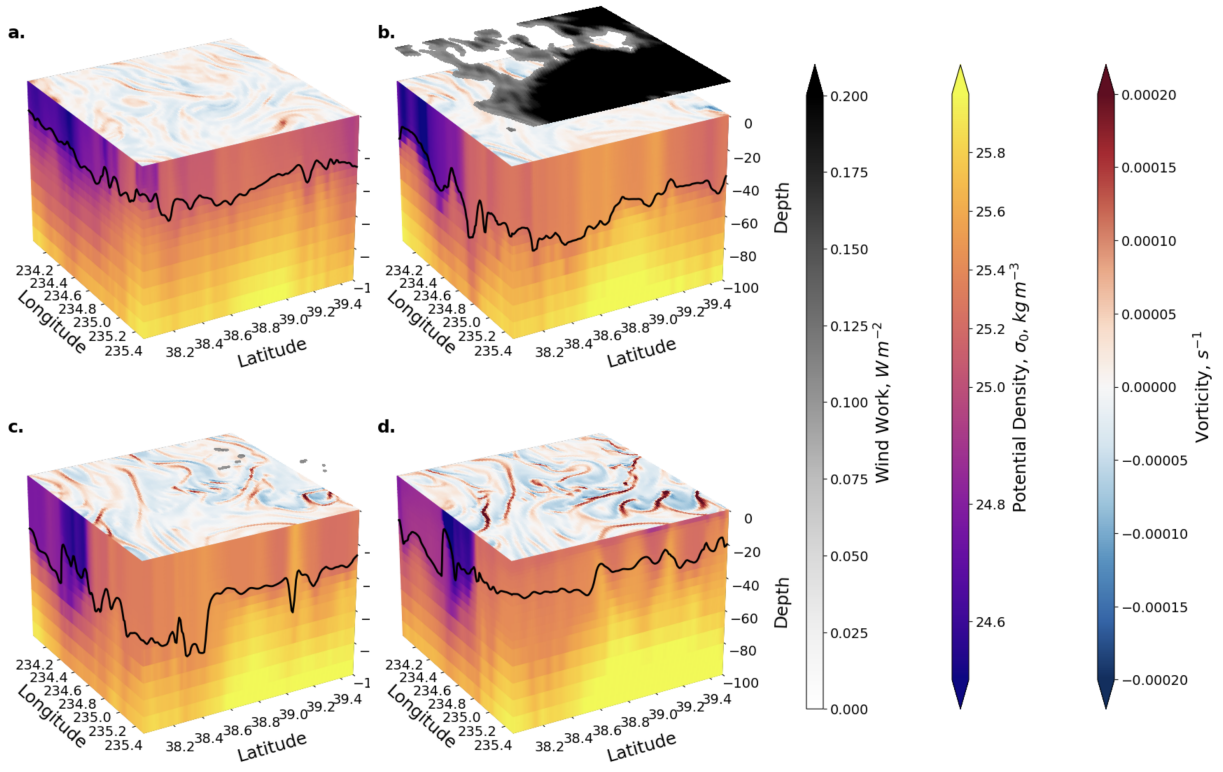


FIG. 4. Snapshots of vorticity at 6 m, with wind work greater than 0.1 W m^{-2} overlaid in gray, with depth faces indicating potential density on a. 22:00, 20 May 2023 b. 11:00, 23 May 2023 c. 11:00, 25 May 2023 d. 00:00, 27 May 2023. Black line indicates mixed-layer depth calculated according to Section 2b.

which peaks approximately four days after the storm-induced wind work (Fig. 5c). The peak submesoscale kinetic energy is further characterized in Figure 5d as energy injection at, and divergence from, scales of approximately 4 km. A portion of this energy cascades downscale to dissipate, while another portion undergoes an inverse cascade, merging into larger eddies and energizing the mesoscale field at scales up to 50 km (Fig. 5e). Cumulative transfer across the 25 km submesoscale–mesoscale boundary (Fig. 5d) closely tracks the submesoscale kinetic energy (Fig. 5c), suggesting the MLI-fed submesoscale reservoir sets the strength of the inverse cascade into the mesoscale. Taken together, these results suggest the hypothesis that mixed-layer instabilities serve as a mechanism by which submesoscale energy is transferred into the mesoscale, with a lag of a few days following the initial storm event.

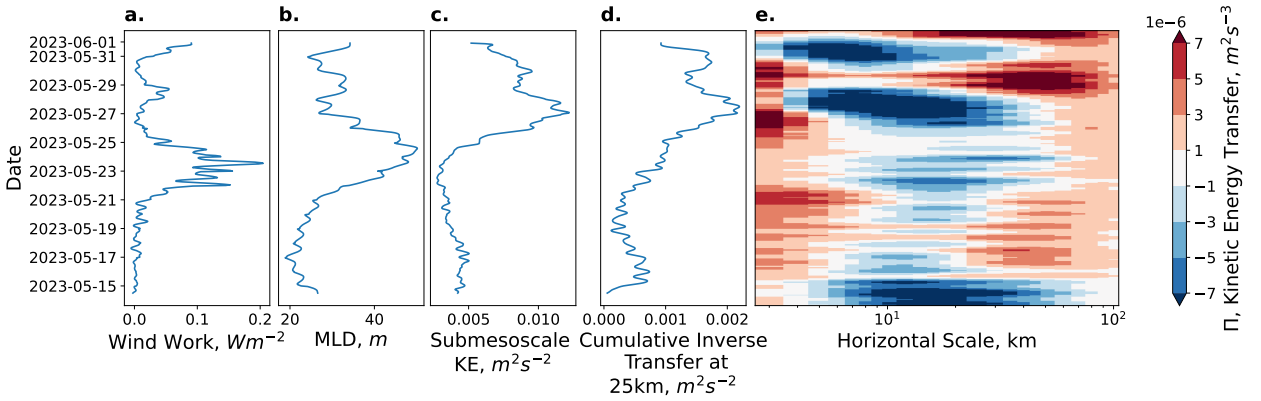


FIG. 5. Spatial mean over 234-235.5° E and 38-39.5° N of a. wind work, b. mixed-layer depth as defined by the potential energy anomaly in Section 2b, c. submesoscale kinetic energy, defined by a dynamical filter that removes the IGWs defined in Section 2e and a subsequent 25-km high-pass filter, d. The cumulative kinetic energy transfer function at 25 km, $\int_{t_0}^{t} \Pi dt$, e. the kinetic energy transfer function, Π, defined using the coarse-graining method outlined in Section 2d. Positive values indicate downscale kinetic energy transfer.

2) Composite Analysis of MLIs in the CCS

These deepening–restratification sequences occur throughout the time series but are most common and energetic during late winter and early spring, coinciding with the period of deepest mixed layers and strongest absolute wind forcing. To isolate the general statistical behavior of these events, we construct a composite analysis for mixed-layer instabilities. We first compute the change in MLD over 5-hour periods, and then extract the most negative 1% of this variable to represent the strongest restratification events. We then screen these events to satisfy the additional conditions: (a) the event center is a maximum in a spatial radius 30 km and temporal radius 120 hours, and (b) any events that share the same geographic center must be separated by at least 120 hours in time. These separation criteria are necessary in order to ensure that the same events are not double counted allowing them to be treated as independent realizations. As such, the spatial and temporal separation criteria of 30 km and 120 hours were chosen to be greater than the Rossby radius of deformation and the duration of the case study MLI (Fig. 5), respectively. The sensitivity to varying these parameters around the chosen values is qualitatively small. Restratification was chosen as the parameter used to define the composite in order to align with the definition of MLIs used by Boccaletti et al. (2007) as a mechanism for restratification of the mixed layer.

Figure 6a shows the distribution of the 336 events in the domain spanning 230–236°E and 35–40°N over the 7-month time series. The events are heavily concentrated during winter and spring and are subdued in summer, although not completely absent. Figures 6b–e show the same bulk statistic means as considered in the case study event in Figure 5. The bulk statistics show a similar progression to the example shown in Figure 5, except with a less extreme MLD variation and a compressed time-span. The composite and the individual example reveal several features consistent with the canonical MLI cycle described in earlier studies (Boccaletti et al. 2007; Fox-Kemper et al. 2008). Here, strong winds (Fig. 6b) result in a deepening of the mixed layer, which reaches its deepest values within 1–2 inertial periods (1 day) after the peak wind work (Fig. 6c). A sharp peak in submesoscale kinetic energy emerges with a delay of 1 day (Fig. 6d). Concurrent with the peak submesoscale kinetic energy is a decreased dominant energy injection scale and a strong inverse cascade at smaller scales (Fig. 6e). As this energy cascades upscale, the submesoscale kinetic energy decreases.

Both the composite (Fig. 6) and the case study (Figs. 3–5) demonstrate that mixed-layer deepening events in the CCS are commonly followed by enhanced submesoscale activity and restratification consistent with MLI dynamics. These events occur throughout the year but cluster in periods of deeper mixed layers, consistent with the hypothesis that the elevated wintertime submesoscale kinetic energy shown in Section 3a is due to enhanced MLIs. Their cumulative effect, and the seasonal changes in their frequency and intensity, underpin the seasonal cycles of submesoscale kinetic energy, mesoscale kinetic energy, and their exchange, which we quantify in Section 3c.

c. Momentum Trapping and Baroclinic Instability

Figure 1c–d highlights a pronounced seasonal contrast in the mean kinetic energy, with substantially stronger currents during summer. A plausible explanation for this behavior is momentum trapping (Peng et al. 2022), whereby increased upper-ocean stratification confines wind-driven momentum to a shallower mixed layer, reducing the effective inertia of the forced layer and allowing the same wind stress to generate faster currents.

Figure 7a shows the time-integrated terms of the geostrophic kinetic energy budget described in Section 2f. The ageostrophic-to-geostrophic transfer term (orange line, Fig. 7a) is a proxy for the inverse transfer of energy from mixed-layer instabilities, which we compare directly to the inverse

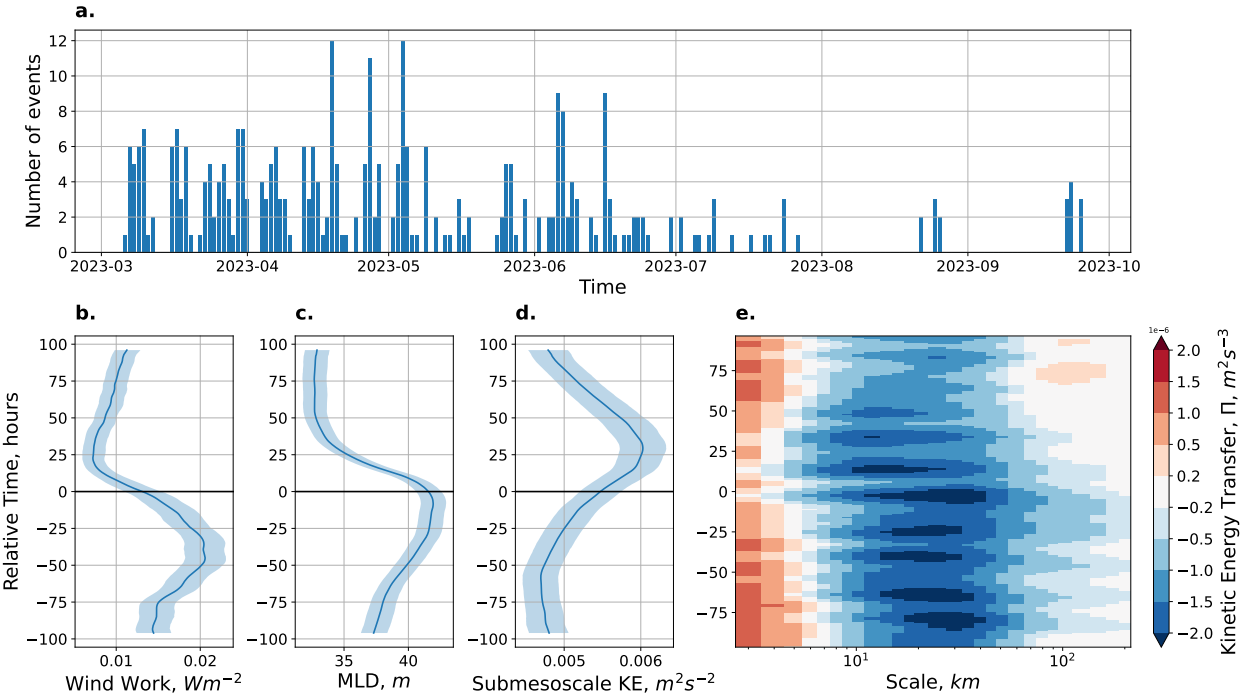
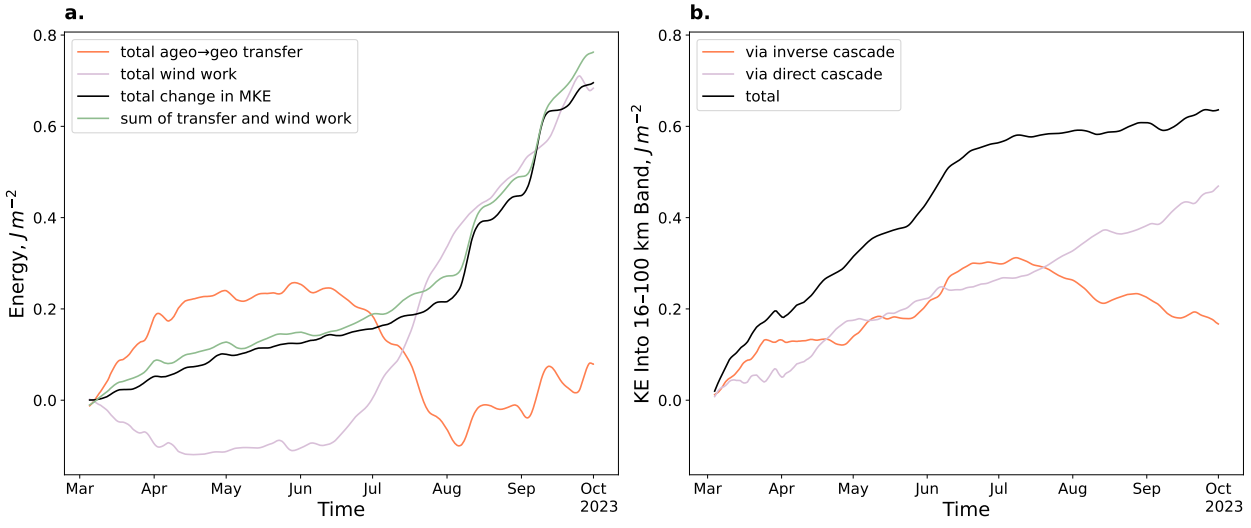


FIG. 6. a. Temporal distribution of mixed-layer instability events included in composite. Composite means over a radius of 30km around the event center with shading indicating the 95% bootstrapped confidence interval of b. wind work, c. mixed-layer depth, defined by the potential energy anomaly in Section 2b, d. submesoscale kinetic energy, defined by a dynamical filter that removes the IGWs and a subsequent 25-km high-pass filter. Composite disk-mean of e. the kinetic energy transfer function, Π, defined using the coarse-graining method outlined in Section 2d

.

kinetic energy transfer across 16 km (orange line, Fig. 7b) This transfer increases through spring (March–May) and peaks in early summer (June), coincident with the period when mixed-layer instabilities rapidly decline in frequency (Fig. 6a). Beyond this point, the sign reversal of the transfer indicates a regime shift in which ageostrophic motions act as a net sink of geostrophic kinetic energy rather than a source.

We hypothesize that the negative wind work in spring (Fig. 7a, purple line) reflects eddy killing, whereby the relative-velocity dependence of the surface stress damps the eddy-dominated winter circulation and returns kinetic energy to the atmosphere (Rai et al. 2021). This dominates during the winter because the California Current itself is less coherent and made up largely of mesoscale eddies in spring/winter (Fig. 1c). As the basin-scale current strengthens into summer (Fig. 1d), eddy



409 FIG. 7. a. 4-day running mean of time-integrated terms in the geostrophic mixed-layer averaged budget
410 averaged over the domain spanning 35.5-39.5°N and 231-235°E: total transfer from ageostrophic motions to
411 geostrophic motions Π_g (orange), total wind work into the ocean per unit depth W_g (purple), sum of both
412 ageostrophic to geostrophic energy transfer and wind work $\Pi_g + W_g$ (green) and change in geostrophic kinetic
413 energy $\int DK_g/Dtdt$ (black). b. Mixed-layer integrated kinetic energy transfer function into the 16-100-km band
414 averaged over 230–235° E and 30–42° N from scales >100 km (purple) and scales <16 km (orange), and their
415 sum (black).

397 killing weakens and the cumulative wind work per unit mixed-layer depth (purple line in Fig. 7a)
398 instead increases steadily from early summer onward, despite a decrease in the absolute wind work
399 as the year progresses. Cumulative wind work becomes the leading-order contributor to changes
400 in kinetic energy during the shallow mixed layer season (July–October). The close agreement
401 between the sum of wind work and ageostrophic–geostrophic transfer (green line, Figure 7a) and the
402 diagnosed change in kinetic energy (black line, Figure 7a) demonstrates that these terms dominate
403 the seasonal budget. Importantly, during summer the balance is overwhelmingly controlled by
404 wind work, consistent with the momentum-trapping hypothesis: as the mixed layer shoals, wind
405 stress becomes a more efficient pathway for energy input, accelerating the mixed-layer current and
406 strengthening the large-scale flow. This summertime strengthening follows the enhanced-upwelling
407 spin-up noted by Di Lorenzo (2003), occurring after the upwelling-favorable winds relax and the
408 mixed layer shoals offshore.

In summer, enhanced stratification strengthens the large-scale current, increasing the energy available for transfer to the mesoscale. Figure 7b shows the cumulative kinetic energy transfer (defined by equation 4) into the 16–100-km band, decomposed by source scale using the coarse-grained energy flux Π. The mesoscale band was chosen to be 16–100 km based on the maximum cumulative kinetic energy transfer from submesoscales up into the mesoscale (16 km) and from the large-scale current system downscale into the mesoscale (100 km). This 16-km boundary, identified as the scale of maximum upscale transfer, lies close to the 25-km first baroclinic Rossby radius scale used a priori to separate submesoscale and mesoscale balanced motions in Section 2e, and the seasonal evolution of the transfer is qualitatively insensitive to which of these two scales is used. Energy transferred from submesoscales (orange line in Figure 7b) increases through spring and peaks in early summer, consistent with active mixed-layer instabilities, but subsequently weakens as enhanced stratification suppresses mixed-layer instability generation. This submesoscale source term, computed directly from the coarse-grained flux, closely tracks the ageostrophic-to-geostrophic transfer (orange line, Fig. 7a); both increase through spring, peak in early summer, and decline thereafter. The agreement is consistent with the hypothesis that the ageostrophic-to-geostrophic term provides a reliable proxy for the MLI-driven inverse cascade. Energy transferred from the large-scale flow (purple line, Fig. 7b) increases steadily throughout the year and exhibits a marked increase in slope around July, implying a more efficient downscale transfer into the mesoscale during summer.

This behavior suggests a transition in the dominant pathway supplying mesoscale kinetic energy: from an inverse transfer driven by submesoscale mixed-layer instabilities in spring to a strengthened direct transfer from the intensified large-scale current in summer. The strengthened current is associated with enhanced horizontal strain, promoting mesoscale baroclinic instability that converts large-scale kinetic energy into mesoscale eddies. The persistence and acceleration of the large-scale–to–mesoscale transfer despite declining submesoscale input highlights the central role of the summer mean flow in maintaining mesoscale activity.

d. Two Pathways to Mesoscale Kinetic Energy

The results presented in Sections 3b and 3c indicate that mesoscale eddies in the CCS are energized by two dynamically distinct pathways whose relative importance varies seasonally:

an inverse transfer from submesoscales driven by mixed-layer instabilities during winter and spring, and a direct transfer from the intensified large-scale flow during summer, consistent with mesoscale baroclinic instability. Previous studies have established that both submesoscale mixed-layer instabilities and mesoscale baroclinic instability are active in boundary current systems (Boccaletti et al. 2007; Capet et al. 2008a,b; Rocha et al. 2016), and have suggested that MLIs can contribute to mesoscale variability through upscale energy transfer (Capet et al. 2008a; Schubert et al. 2020; Sasaki et al. 2014). However, the seasonal variation in relative importance of these processes, and how they jointly shape the mesoscale energy budget in the CCS, has remained less clearly quantified.

Figure 7b directly quantifies the seasonal partition of energy supply into the mesoscale band using the coarse-grained flux Π, decomposed by source scale. Energy transferred from submesoscales (< 16 km) increases through spring and peaks in early summer, consistent with active mixed-layer instabilities and the composite evolution described in Section 3b: mixed-layer deepening events generate intense submesoscale eddies which subsequently merge through an inverse cascade, transferring energy upscale into the mesoscale band (Capet et al. 2008a; Schubert et al. 2020; Sasaki et al. 2014). In contrast, energy transferred from the large-scale flow (> 100 km) increases steadily throughout the year and exhibits a marked increase in slope around July, indicating the onset of a more efficient downscale transfer into the mesoscale during summer. This timing coincides with the shallow mixed-layer season (Fig. 1e) and with the increasing importance of wind work per unit mixed-layer depth in the geostrophic budget (Fig. 7a), consistent with momentum trapping (Peng et al. 2022) strengthening the large-scale flow and increasing the energy available for transfer to the mesoscale.

The seasonal transition in the dominant source is also evident in the full, time-scale evolution of Π (Fig. 8a). During winter and spring, Π exhibits frequent, patchy negative anomalies representing inverse cascades, consistent with intermittent but intense upscale transfer associated with restratification events and mixed-layer instabilities. These events become less frequent and weaker in summer, coincident with the suppression of submesoscale activity. With the lack of a small-scale energy injection scale in summer, the direct cascade to dissipation extends up to larger scales and is part of the reason for the submesoscale becoming a sink for the mesoscale rather than a source. Consistent with Tedesco et al. (2023), we find that daily averaging largely suppresses the direct cas-

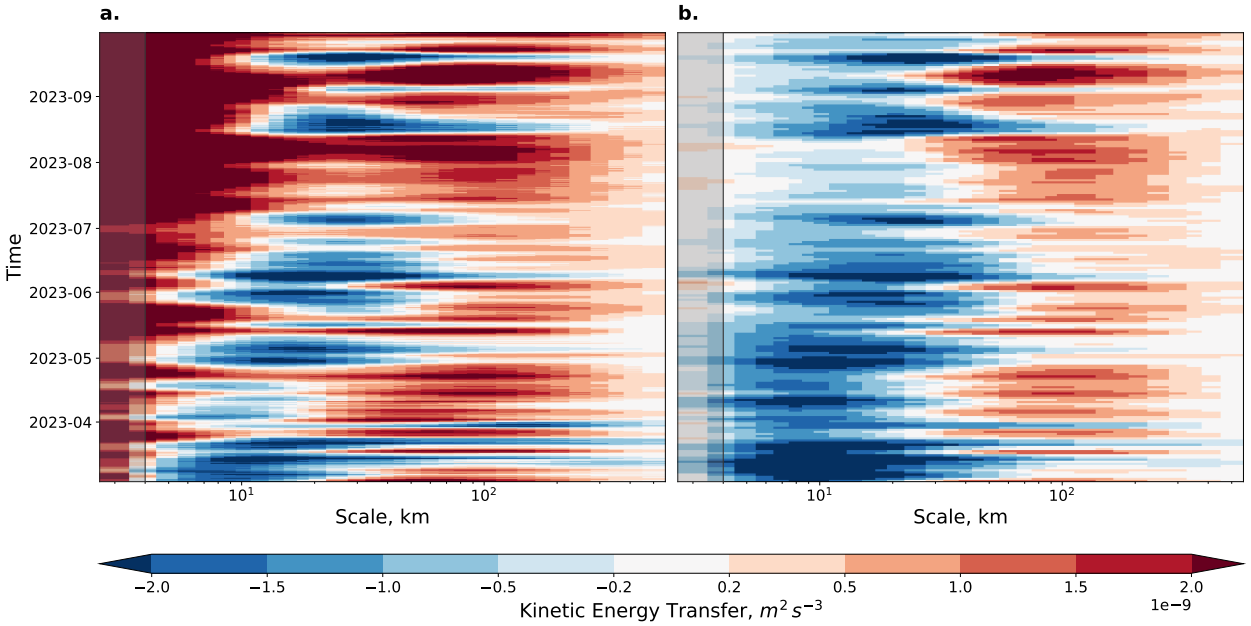
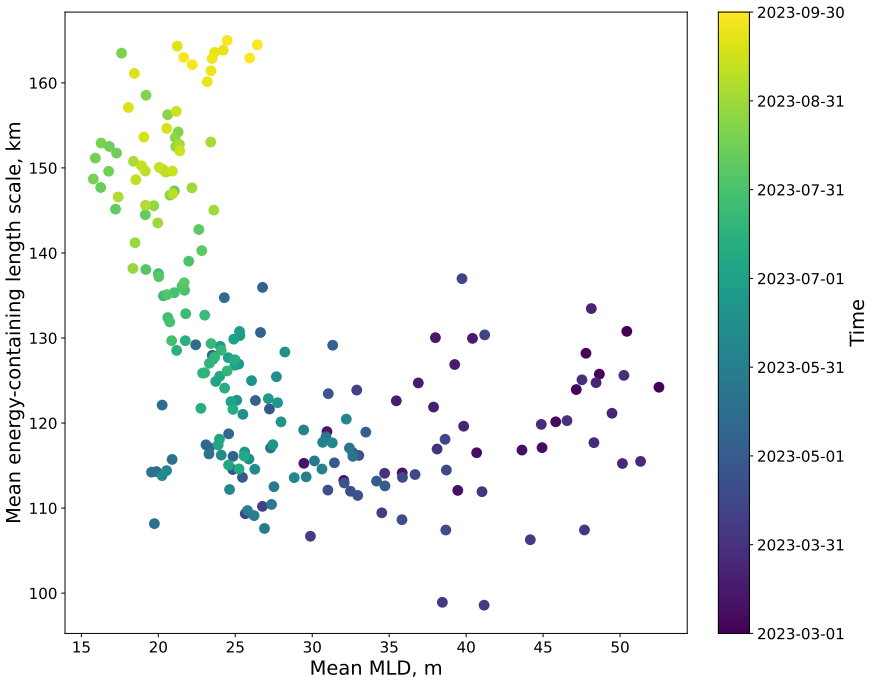


FIG. 8. A 72-hour rolling average of the mean kinetic energy transfer function, Π, averaged over 230–235° E and 30–42° N using a) hourly data and b) daily-averaged data. In both panels, shading represents scales ≤ 4 km, the effective resolution of the model, and values in this shaded region are not significant.

cade to dissipation (Fig. 8b), indicating that a substantial fraction of the turbulent energy transfer to dissipative scales resides at high temporal frequencies. Persistent positive Π anomalies are present at scales of 100–200 km, but they intensify as the year goes on, reflecting a strengthening direct cascade from the mean current and large mesoscale features into the mesoscale band.Figures 7b and 8 show a convergence of energy into the mesoscale band from both larger and smaller scales, with the source partitioning shifting from predominantly submesoscale in spring to predominantly large-scale in summer.

This source shift provides a natural interpretation of the seasonal change in characteristic eddy scale. Figure 9 shows the mean energy-containing eddy scale, computed as the integral over the variance-preserving wavenumber spectrum, plotted against the domain-mean mixed-layer depth. During winter and spring (purple and blue dots), the two quantities are not related, reflecting a regime in which mesoscale variability is energized from smaller scales by an inverse cascade that is largely controlled by intermittent, local restratification events. Beginning in early summer (green and yellow dots), however, the two become tightly correlated, with shoaling mixed layers associated with a systematic increase in eddy scale. This transition coincides with the onset of



485 FIG. 9. Daily mean energy containing length scale, calculated as the integral over the variance-preserving
486 wavenumber spectrum vs daily mean mixed-layer depth.

495 strong momentum trapping (Section 3c), whereby wind-driven energy input becomes increasingly
496 confined to the shallow mixed layer, amplifying the large-scale current. The intensified current
497 strengthens lateral buoyancy gradients and horizontal strain, promoting mesoscale baroclinic in-
498 stability that directly transfers kinetic energy from the mean flow to the mesoscale eddies while
499 acting to relax buoyancy gradients imposed by the straining flow.

500 4. Discussion and Conclusion

501 This study has quantified the seasonal mechanisms that supply kinetic energy to the mesoscale
502 band $O(100$ km) in the California Current System, using a high-resolution simulation and a suite
503 of energetics diagnostics. The results show that the CCS mesoscale band is maintained through
504 two dynamically distinct pathways whose relative importance shifts over the seasonal cycle: an
505 inverse transfer from submesoscales associated with mixed-layer instabilities during winter and
506 spring, and a direct transfer from the intensified large-scale flow during summer.

507 An important implication is that the mesoscale band in the CCS functions as an intermediate
508 reservoir that can be supplied by energy from both smaller and larger scales, with the balance

between these sources varying seasonally. This behavior is consistent with theoretical expectations for geostrophic turbulence in which both upscale and downscale transfers may coexist depending on the structure of forcing and dissipation (Vallis 2017; Aluie et al. 2018). It also helps reconcile two previously emphasized perspectives in the literature: one in which mesoscale variability is influenced by submesoscale mixed-layer processes (Boccaletti et al. 2007; Capet et al. 2008a; Rocha et al. 2016), and another in which mesoscale energy is primarily derived from instabilities of the large-scale circulation (Vallis 2017). In the CCS, both pathways are active, but their relative roles depend strongly on seasonal stratification and mixed-layer depth. The framework developed here therefore provides a basis for interpreting seasonal mesoscale variability in terms of underlying energy pathways, and for comparative application to other boundary current systems where mixed-layer depth and storm forcing vary strongly over the seasonal cycle (Rocha et al. 2016; Brannigan et al. 2015; Qiu et al. 2014; Sasaki et al. 2014). A further goal is to identify whether a critical mixed-layer depth or stratification threshold governs the regime shift between submesoscale-driven inverse transfer and large-scale-driven direct transfer.

The cross-scale energy transfer diagnosed here can be contrasted with that reported by Capet et al. (2008c), whose idealized CCS simulations were forced by steady, time-invariant forcing with no synoptic or seasonal variability. In their simulations, the kinetic energy injection is around the Rossby radius and their spectral flux is inverse at mesoscale wavelengths, consistent with geostrophic turbulence, but reverses near a 30 km wavelength so that the submesoscale exhibits a forward cascade and acts as a sink draining mesoscale energy toward dissipation. Both their solutions and ours thus contain an inverse cascade around the mesoscale; the difference lies in the role of the submesoscale and the scale at which the inverse cascade begins. During spring, we find that MLIs inject submesoscale KE that is transferred upscale, so that the submesoscale is a source rather than a sink for the mesoscale and the inverse cascade extends to scales well below the transition found by Capet et al. (2008c). We interpret this not as a contradiction but as direct support for our central hypothesis. Figure 6b shows that the MLIs responsible require spatiotemporally variable wind forcing that deepens the mixed layer and sharpens the lateral buoyancy gradients released upon restratification, a cycle that the steady forcing of Capet et al. (2008c) cannot generate. In its absence the submesoscale is energized only through mesoscale straining and frontogenesis and the inverse cascade is confined to the mesoscale, whereas the variable forcing of the real CCS

shifts the inverse cascade to smaller scales and intensifies the upscale supply to the mesoscale. The contrast is consistent with the hypothesis that atmospheric variability generates MLIs that govern the scale range and strength of the inverse cascade energizing the mesoscale in the CCS.

The results presented here also suggest that mesoscale variability in the CCS may be sensitive to long-term changes in stratification and atmospheric forcing. Increased upper-ocean stratification associated with surface warming would favor shallower mixed layers and potentially enhance the efficiency of momentum trapping, strengthening the large-scale pathway for mesoscale energization. Conversely, changes in storm frequency or intensity would be expected to modulate the prevalence of deepening–restratification events and therefore the contribution of the MLI pathway. For the North Pacific, potential changes in large-scale atmospheric circulation may therefore influence mesoscale variability in the CCS by changing the frequency and intensity of deepening–restratification events due to storms—and hence the relative contribution of the two pathways outlined in this research. Understanding how these competing effects evolve under climate change remains an open question.

Recent observations from the Sub-Mesoscale Ocean Dynamics Experiment (S-MODE) provide an important observational context for the mechanisms identified here. The presence of an energetic field of submesoscale fronts, filaments, and vortices in the California Current region west of central California was reported, demonstrating that the upper ocean supports vigorous submesoscale variability embedded within a broader mesoscale circulation (Farrar et al. 2025). Airborne DopplerScatt measurements during S-MODE revealed rapidly evolving 1–20 km features with Rossby number and divergence normalized by the Coriolis frequency of order unity and inferred vertical velocities exceeding 200 m day^{-1} at tens of meters depth (Torres et al. 2024). These observations are qualitatively consistent with the winter–spring regime identified here, in which deep mixed layers and storm-driven forcing favor mixed-layer instabilities that inject energy at submesoscales, resulting in a vigorous submesocale field. However, the results from DopplerScatt suggest a more energetic submesoscale field with a spectral slope of $\sim k^{-2}$ compared with this study in which we find a $\sim k^{-3}$ slope. We hypothesize that the disagreement in spectral slope occurs because the DopplerScatt measurements are higher resolution and resolve more of the submesoscale field. A similar contrast holds with the simulations of Capet et al. (2008c), which show a comparably shallow $\sim k^{-2}$ submesoscale slope. Dynamically, this difference is consistent

with the differing configurations of the models. Capet et al. (2008c) force the simulations with idealized, steady forcing sustaining perpetual frontogenesis in a weakly stratified mixed-layer, a state our simulation never reaches. In summer, when the submesoscales are suppressed by increased stratification our spectral slope steepens to $\sim k^{-4}$. However, here, the dynamics have shifted even further from the forced conditions in Capet et al. (2008c). Numerically, the effective resolution of our simulation could also contribute to the difference in spectral slope. Subgridscale submesoscale motions could therefore be underrepresented in the simulated velocity field, and their omission may lead to an underestimate of the magnitude of the inverse kinetic energy transfer from submesoscales into the mesoscale band. The contribution of mixed-layer instabilities to the mesoscale kinetic energy budget inferred here may represent a lower bound. Future work could combine DopplerScatt velocity measurements with coarse-grained kinetic energy diagnostics to directly quantify cross-scale energy transfers at smaller spatial scales and assess their contribution to mesoscale energization in the California Current System.

A further consideration is the model's effective resolution, approximately a few gridpoints or ~4 km, which is close to the scale at which mixed-layer instabilities inject kinetic energy during winter and spring (Fig. 8). Cross-scale transfers at and below this scale are correspondingly less well constrained, as indicated by the shading in Figure 8. However, our central conclusions rest on the resolved cross-scale transfers diagnosed from the coarse-grained flux Π, and in particular the transfer into the well-resolved 16–100 km band (Fig. 7b).

Quantifying the balance between upscale and downscale cascades under different forcing regimes may help resolve long-standing questions about energy transfer in the ocean. The framework presented here could be applied to other systems, such as the Kuroshio Extension, the Gulf Stream, or the Antarctic Circumpolar Current, where the seasonal cycle of stratification or storms are also important. Based on the results of this study, we hypothesize that in more energetic Western boundary current systems, the MLI pathway will be enhanced, particularly in areas with high variance in stratification.

Acknowledgments. We thank Dr. Hector Torres for providing code for dynamical filtering. JFG and STG acknowledge support from NASA contract 80GSFC24CA067. JFG, STG, and SPX were also supported through a subaward from Remote Sensing Systems for NASA award 80NSSC22M0010. STG also acknowledges support from NASA awards 80NSSC21K1822 and 80NSSC24K1657. LS acknowledges support from NASA grant 80NSSC24K1653. ACNG acknowledges support from the UK Natural Environment Research Council (grant NE/W009501/1). JM and JA acknowledge funding by the Naval Research Laboratory base program Ocean Submesoscale Eddy Evolution. This paper is contribution NRL/7320/JA–2026/3 and has been approved for public release.

Data availability statement. Processed intermediate data files are available through the UC San Diego Library Digital Collections (DOI: https://doi.org/10.6075/J0DF6S64), along with the code used to generate the figures in this study. The intermediate files primarily consist of variables extracted from the raw NCOM output, in some cases with additional temporal averaging or derived calculations required for figure generation. Details of the processing, averaging, and derived quantities are provided in the accompanying README file.

References

Allard, R., E. Rogers, P. Martin, T. Jensen, and P. Chu, 2015: The US Navy Coupled Ocean-Wave Prediction System. *Oceanography*, **27 (3)**, 92–102, https://doi.org/10.5670/oceanog.2014.71, URL https://tos.org/oceanography/article/the-us-navy-coupled-ocean-wave-prediction-system.

Aluie, H., M. Hecht, and G. K. Vallis, 2018: Mapping the Energy Cascade in the North Atlantic Ocean: The Coarse-Graining Approach. *Journal of Physical Oceanography*, **48 (2)**, 225–244, https://doi.org/10.1175/JPO-D-17-0100.1, URL https://journals.ametsoc.org/view/journals/phoc/48/2/jpo-d-17-0100.1.xml.

Asselin, O., and W. R. Young, 2020: Penetration of Wind-Generated Near-Inertial Waves into a Turbulent Ocean. *Journal of Physical Oceanography*, **50 (6)**, 1699–1716, https://doi.org/10.1175/JPO-D-19-0319.1, URL https://journals.ametsoc.org/view/journals/phoc/50/6/JPO-D-19-0319.1.xml.

Barron, C. N., A. B. Kara, P. J. Martin, R. C. Rhodes, and L. F. Smedstad, 2006: Formulation, implementation and examination of vertical coordinate choices in the Global Navy Coastal Ocean Model (NCOM). *Ocean Modelling*, **11 (3)**, 347–375, https://doi.org/10.1016/j.ocemod.2005.01.004, URL https://www.sciencedirect.com/science/article/pii/S1463500305000120.

Barron, C. N., and L. F. Smedstad, 2002: Global river inflow with Navy Coastal Ocean Model. *OCEANS'02 MTS/IEEE*, IEEE, Vol. 3, 1472–1479, URL https://ieeexplore.ieee.org/abstract/document/1191855/.

Boccaletti, G., R. Ferrari, and B. Fox-Kemper, 2007: Mixed Layer Instabilities and Restratification. *Journal of Physical Oceanography*, **37 (9)**, 2228–2250, https://doi.org/10.1175/JPO3101.1, URL https://journals.ametsoc.org/view/journals/phoc/37/9/jpo3101.1.xml.

Brannigan, L., D. P. Marshall, A. Naveira-Garabato, and A. J. George Nurser, 2015: The seasonal cycle of submesoscale flows. *Ocean Modelling*, **92**, 69–84, https://doi.org/10.1016/j.ocemod.2015.05.002, URL https://www.sciencedirect.com/science/article/pii/S1463500315000803.

Buckingham, C. E., and Coauthors, 2016: Seasonality of submesoscale flows in the ocean surface boundary layer. *Geophysical Research Letters*, **43 (5)**, 2118–2126, https://doi.org/10.1002/2016GL068009, URL https://onlinelibrary.wiley.com/doi/abs/10.1002/2016GL068009.

Callies, J., R. Ferrari, J. M. Klymak, and J. Gula, 2015: Seasonality in submesoscale turbulence. *Nature Communications*, **6**, https://doi.org/DOI:10.1038/ncomms7862, URL https://www.nature.com/articles/ncomms7862.

Capet, X., J. C. McWilliams, M. J. Molemaker, and A. F. Shchepetkin, 2008a: Mesoscale to Submesoscale Transition in the California Current System. Part I: Flow Structure, Eddy Flux, and Observational Tests. *Journal of Physical Oceanography*, **38 (1)**, 29–43, https://doi.org/10.1175/2007JPO3671.1, URL https://journals.ametsoc.org/view/journals/phoc/38/1/2007jpo3671.1.xml.

Capet, X., J. C. McWilliams, M. J. Molemaker, and A. F. Shchepetkin, 2008b: Mesoscale to Submesoscale Transition in the California Current System. Part II: Frontal Processes. *Journal of Physical Oceanography*, **38 (1)**, 44–64, https://doi.org/10.1175/2007JPO3672.1, URL https://journals.ametsoc.org/view/journals/phoc/38/1/2007jpo3672.1.xml.

Capet, X., J. C. McWilliams, M. J. Molemaker, and A. F. Shchepetkin, 2008c: Mesoscale to Submesoscale Transition in the California Current System. Part III: Energy Balance and Flux. *Journal of Physical Oceanography*, **38 (10)**, 2256–2269, https://doi.org/10.1175/2008JPO3810.1, URL https://journals.ametsoc.org/view/journals/phoc/38/10/2008jpo3810.1.xml.

Charney, J. G., 1971: Geostrophic Turbulence. *Journal of the Atmospheric Sciences*, **28 (6)**, 1087–1095, https://doi.org/10.1175/1520-0469(1971)028⟨1087:GT⟩2.0.CO;2, URL https://journals.ametsoc.org/view/journals/atsc/28/6/1520-0469_1971_028_1087_gt_2_0_co_2.xml.

Chelton, D. B., R. A. deSzoeke, M. G. Schlax, K. E. Naggar, and N. Siwertz, 1998: Geographical Variability of the First Baroclinic Rossby Radius of Deformation. *Journal of Physical Oceanography*, **28 (3)**, 433–460, https://doi.org/10.1175/1520-0485(1998)028⟨0433:GVOTFB⟩2.0.CO;2, URL https://journals.ametsoc.org/view/journals/phoc/28/3/1520-0485_1998_028_0433_gvotfb_2.0.co_2.xml.

Cummings, J. A., 2005: Operational multivariate ocean data assimilation. *Quarterly Journal of the Royal Meteorological Society*, **131 (613)**, 3583–3604, https://doi.org/10.1256/qj.05.105, URL https://onlinelibrary.wiley.com/doi/abs/10.1256/qj.05.105.

Cummings, J. A., S. Smith, S. N. Carroll, and P. Spence, 2010: User's Manual for the Navy Coupled Ocean Data Assimilation 3D Variational Analysis (NCODA 3DVar) System, Version 3.0. URL https://apps.dtic.mil/sti/html/trecms/AD1134364/index.html.

D'Addezio, J. M., S. Smith, G. A. Jacobs, R. W. Helber, C. Rowley, I. Souopgui, and M. J. Carrier, 2019: Quantifying wavelengths constrained by simulated SWOT observations in a submesoscale resolving ocean analysis/forecasting system. *Ocean Modelling*, **135**, 40–55, https://doi.org/10.1016/j.ocemod.2019.02.001, URL https://www.sciencedirect.com/science/article/pii/S1463500318302166.

Daley, R., and E. Barker, 2001: NAVDAS: Formulation and Diagnostics. *Monthly Weather Review*, **129 (4)**, 869–883, https://doi.org/10.1175/1520-0493(2001)129⟨0869:NFAD⟩2.0.CO;2, URL https://journals.ametsoc.org/view/journals/mwre/129/4/1520-0493_2001_129_0869_nfad_2.0.co_2.xml.

Di Lorenzo, E., 2003: Seasonal dynamics of the surface circulation in the Southern California Current System. *Deep Sea Research Part II: Topical Studies in Oceanography*, **50 (14)**, 2371–2388, https://doi.org/10.1016/S0967-0645(03)00125-5, URL https://www.sciencedirect.com/science/article/pii/S0967064503001255.

Egbert, G. D., and S. Y. Erofeeva, 2002: Efficient Inverse Modeling of Barotropic Ocean Tides. *Journal of Atmospheric and Oceanic Technology*, **19 (2)**, 183–204, https://doi.org/10.1175/1520-0426(2002)019⟨0183:EIMOBO⟩2.0.CO;2, URL https://journals.ametsoc.org/view/journals/atot/19/2/1520-0426_2002_019_0183_eimobo_2_0_co_2.xml.

Farrar, J. T., and Coauthors, 2025: S-MODE: The Sub-Mesoscale Ocean Dynamics Experiment. *Bulletin of the American Meteorological Society*, **106 (4)**, E657–E677, https://doi.org/10.1175/BAMS-D-23-0178.1, URL https://journals.ametsoc.org/view/journals/bams/106/4/BAMS-D-23-0178.1.xml.

Ferrari, R., and M. Nikurashin, 2010: Suppression of Eddy Diffusivity across Jets in the Southern Ocean. *Journal of Physical Oceanography*, **40 (7)**, 1501–1519, https://doi.org/10.1175/2010JPO4278.1, URL https://journals.ametsoc.org/view/journals/phoc/40/7/2010jpo4278.1.xml.

Ferrari, R., and C. Wunsch, 2009: Ocean Circulation Kinetic Energy: Reservoirs, Sources, and Sinks. *Annual Review of Fluid Mechanics*, **41 (Volume 41, 2009)**, 253–282, https://doi.org/10.1146/annurev.fluid.40.111406.102139, URL https://www.annualreviews.org/content/journals/10.1146/annurev.fluid.40.111406.102139.

Fox-Kemper, B., R. Ferrari, and R. Hallberg, 2008: Parameterization of Mixed Layer Eddies. Part I: Theory and Diagnosis. *Journal of Physical Oceanography*, **38 (6)**, 1145–1165, https://doi.org/10.1175/2007JPO3792.1, URL https://journals.ametsoc.org/view/journals/phoc/38/6/2007jpo3792.1.xml.

Hogan, T. F., M. Liu, J. A. Ridout, M. S. Peng, and T. R. Whitcomb, 2015: The Navy Global Environmental Model. *Oceanography*, **27 (3)**, 116–125, https://doi.org/10.5670/oceanog.2014.73, URL https://tos.org/oceanography/article/the-navy-global-environmental-model.

Holte, J., L. D. Talley, J. Gilson, and D. Roemmich, 2017: An Argo mixed layer climatology and database. *Geophysical Research Letters*, **44 (11)**, 5618–5626, https://doi.org/10.1002/2017GL073426, URL https://onlinelibrary.wiley.com/doi/abs/10.1002/2017GL073426.

Khatri, H., S. M. Griffies, T. Uchida, H. Wang, and D. Menemenlis, 2021: Role of Mixed-Layer Instabilities in the Seasonal Evolution of Eddy Kinetic Energy Spectra in a Global Submesoscale Permitting Simulation. *Geophysical Research Letters*, **48 (18)**, https://doi.org/10.1029/2021GL094777, URL https://onlinelibrary.wiley.com/doi/abs/10.1029/2021GL094777.

McGillicuddy, D. J., and Coauthors, 2007: Eddy/Wind Interactions Stimulate Extraordinary Mid-Ocean Plankton Blooms. *Science*, **316 (5827)**, 1021–1026, https://doi.org/10.1126/science.1136256, URL https://www.science.org/doi/10.1126/science.1136256.

Mellor, G. L., and T. Yamada, 1982: Development of a turbulence closure model for geophysical fluid problems. *Reviews of Geophysics*, **20 (4)**, 851–875, https://doi.org/10.1029/RG020i004p00851, URL https://onlinelibrary.wiley.com/doi/abs/10.1029/RG020i004p00851.

Metzger, E. J., O. M. Smedstad, P. G. Thoppil, H. E. Hurlburt, and J. A. Cummings, 2015: US Navy Operational Global Ocean and Arctic Ice Prediction Systems. *Oceanography*, **27 (3)**, 32–43, https://doi.org/10.5670/oceanog.2014.66, URL https://tos.org/oceanography/article/us-navy-operational-global-ocean-and-arctic-ice-prediction-systems.

Naveira-Garabato, A. C., X. Yu, J. Callies, R. Barkan, K. L. Polzin, E. E. Frajka-Williams, C. E. Buckingham, and S. M. Griffies, 2022: Kinetic Energy Transfers between Mesoscale and Submesoscale Motions in the Open Ocean's Upper Layers. *Journal of Physical Oceanography*, **52 (1)**, 75–97, https://doi.org/10.1175/JPO-D-21-0099.1, URL https://journals.ametsoc.org/view/journals/phoc/52/1/JPO-D-21-0099.1.xml.

Peng, Q., S.-P. Xie, D. Wang, R. X. Huang, G. Chen, Y. Shu, J.-R. Shi, and W. Liu, 2022: Surface warming–induced global acceleration of upper ocean currents. *Science Advances*, **8 (16)**, https://doi.org/10.1126/sciadv.abj8394, URL https://www.science.org/doi/10.1126/sciadv.abj8394.

Qiu, B., S. Chen, P. Klein, H. Sasaki, and Y. Sasai, 2014: Seasonal Mesoscale and Submesoscale Eddy Variability along the North Pacific Subtropical Countercurrent. *Journal of*

Physical Oceanography, **44 (12)**, 3079–3098, https://doi.org/10.1175/JPO-D-14-0071.1, URL https://journals.ametsoc.org/view/journals/phoc/44/12/jpo-d-14-0071.1.xml.

Rai, S., M. Hecht, M. Maltrud, and H. Aluie, 2021: Scale of oceanic eddy killing by wind from global satellite observations. *Science Advances*, **7 (28)**, https://doi.org/10.1126/sciadv.abf4920, URL https://www.science.org/doi/10.1126/sciadv.abf4920.

Reichl, B. G., A. Adcroft, S. M. Griffies, and R. Hallberg, 2022: A Potential Energy Analysis of Ocean Surface Mixed Layers. *Journal of Geophysical Research: Oceans*, **127 (7)**, https://doi.org/10.1029/2021JC018140, URL https://onlinelibrary.wiley.com/doi/abs/10.1029/2021JC018140.

Rocha, C. B., S. T. Gille, T. K. Chereskin, and D. Menemenlis, 2016: Seasonality of submesoscale dynamics in the Kuroshio Extension. *Geophysical Research Letters*, **43 (21)**, 11,304–11,311, https://doi.org/10.1002/2016GL071349, URL https://onlinelibrary.wiley.com/doi/abs/10.1002/2016GL071349.

Sasaki, H., P. Klein, B. Qiu, and Y. Sasai, 2014: Impact of oceanic-scale interactions on the seasonal modulation of ocean dynamics by the atmosphere. *Nature Communications*, **5 (1)**, 5636, https://doi.org/10.1038/ncomms6636, URL https://doi.org/10.1038/ncomms6636.

Schubert, R., J. Gula, R. J. Greatbatch, B. Baschek, and A. Biastoch, 2020: The Submesoscale Kinetic Energy Cascade: Mesoscale Absorption of Submesoscale Mixed Layer Eddies and Frontal Downscale Fluxes. *Journal of Physical Oceanography*, **50 (9)**, 2573–2589, https://doi.org/10.1175/JPO-D-19-0311.1, URL https://journals.ametsoc.org/view/journals/phoc/50/9/jpoD190311.xml.

Smagorinsky, J., 1963: GENERAL CIRCULATION EXPERIMENTS WITH THE PRIMITIVE EQUATIONS: I. THE BASIC EXPERIMENT. *Monthly Weather Review*, **91 (3)**, 99–164, https://doi.org/10.1175/1520-0493(1963)091⟨0099:GCEWTP⟩2.3.CO;2, URL https://journals.ametsoc.org/view/journals/mwre/91/3/1520-0493_1963_091_0099_gcewtp_2_3_co_2.xml.

Tedesco, P. F., L. E. Baker, A. C. N. Garabato, M. R. Mazloff, S. T. Gille, C. P. Caulfield, and A. Mashayek, 2023: Spatiotemporal Characteristics of the Near-Surface Turbulent Cascade at the Submesoscale in the Drake Passage. *Journal of Physical Oceanography*, **54 (1)**,

187–215, https://doi.org/10.1175/JPO-D-23-0108.1, URL https://journals.ametsoc.org/view/journals/phoc/54/1/JPO-D-23-0108.1.xml.

Torres, H. S., P. Klein, D. Menemenlis, B. Qiu, Z. Su, J. Wang, S. Chen, and L.-L. Fu, 2018: Partitioning Ocean Motions Into Balanced Motions and Internal Gravity Waves: A Modeling Study in Anticipation of Future Space Missions. *Journal of Geophysical Research: Oceans*, **123 (11)**, 8084–8105, https://doi.org/10.1029/2018JC014438, URL https://onlinelibrary.wiley.com/doi/abs/10.1029/2018JC014438.

Torres, H. S., and Coauthors, 2022: Separating Energetic Internal Gravity Waves and Small-Scale Frontal Dynamics. *Geophysical Research Letters*, **49 (6)**, e2021GL096 249, https://doi.org/10.1029/2021GL096249, URL https://onlinelibrary.wiley.com/doi/abs/10.1029/2021GL096249.

Torres, H. S., and Coauthors, 2024: Airborne observations of fast-evolving ocean submesoscale turbulence. *Communications Earth & Environment*, **5 (1)**, 771, https://doi.org/10.1038/s43247-024-01917-3, URL https://www.nature.com/articles/s43247-024-01917-3.

Vallis, G. K., 2017: *Atmospheric and Oceanic Fluid Dynamics: Fundamentals and Large-Scale Circulation*. 2nd ed., Cambridge University Press, Cambridge, https://doi.org/10.1017/9781107588417, URL https://www.cambridge.org/core/books/atmospheric-and-oceanic-fluid-dynamics/41379BDDC4257CBE11143C466F6428A4.

Zhang, Y., H. Xu, F. Qiao, and C. Dong, 2018: Seasonal variation of the global mixed layer depth: comparison between Argo data and FIO-ESM. *Frontiers of Earth Science*, **12 (1)**, 24–36, https://doi.org/10.1007/s11707-017-0631-6, URL https://doi.org/10.1007/s11707-017-0631-6.